12,05

Development and characterization of magnetic nanoparticles $Co_{1-x}Zn_xFe_2O_4$ ($0 \leq x \leq 0.6$) for biomedical applications

© A.S. Kamzin[1], I.M. Obaidat[2], V.G. Semenov[3], V. Narayanaswamy[4,5], I.A. Al-Omari[6], B. Issa[4,5,7], I.V. Buryanenko[8]

[1] Ioffe Institute,
St. Petersburg, Russia
[2] Department of Physics, United Arab Emirates University,
Al-Ain 15551, UAE
[3] St. Petersburg State University,
St. Petersburg, Russia
[4] Research Institute of Medical Sharjah,
P.O. Box 27272, UAE
[5] Department of Medical Diagnostic Imaging, College of Health Sciences, University of Sharjah,Sharjah,
P.O. Box 27272, UAE
[6] Department of Physics, Sultan Qaboos University,
P.O. Box 36, Muscat PC 123, Sultanate of Oman
[7] Department of Biomedical Engineering, Faculty of Engineering and Natural Sciences, Istinye University,
Istanbul, 34010, Turkey
[8] Peter the Great Saint-Petersburg Polytechnic University,
St. Petersburg, Russia

E-mail: ASKam@mail.ioffe.ru

Received December 3, 2022
Revised December 3, 2022
Accepted December 6, 2022

The results of studies of the properties of co-deposition of magnetic nanoparticles (MNPs) of $Co_{1-x}Zn_xFe_2O_4$ spinel ferrites synthesized (at $x = 0.0$; 0.1; 0.2; 0.4; 0.6) in order to synthesize magnetic particles for biomedical applications. X-ray diffraction (XRD), raman spectra, magnetic measurements and Mossbauer spectroscopy (MS) were used to study the $Co_{1-x}Zn_xFe_2O_4$ MNPs. It was found that the synthesized MNPs $Co_xZn_{1-x}Fe_2O_4$ are single-phase. According to the results of XRD measurements, it was found that the average sizes of crystallites are 13 nm for $CoFe_2O_4$ ($x = 0$) and, with an increase in the Zn concentration, they decrease to 7 nm for $Co_{1-x}Zn_xFe_2O_4$ ($x = 0.6$), which is consistent with the Mössbauer data, which showed that the sizes of crystallites vary from 14 to 8 nm. In the raman spectra of the $Co_{1-x}Zn_xFe_2O_4$ MNPs in the region of $\sim 620\,cm^{-1}$, splitting of the A_{1g}, line is observed, indicating that the studied particles have an inverse spinel structure. The change in the ratio between intensities of A_{1g} (1) and A_{1g} (2) peaks is indicative of a significant redistribution of Co^{2+} and Fe^{3+} cations between tetrahedral and octahedral positions in $Co_{1-x}Zn_xFe_2O_4$ MNPs as the quantity of Zn increases, which is confirmed by the Mössbauer data. It is found that small sizes of MNPs result in a strengthening of the effects of size and an effect of surface on the magnetic structure of the surface layer. The MS analysis has shown that there is a layer on the MNP surface, the magnetic structure of which is different from from the structure of the crystallite volume. With increase in the quantity of Zn ions thickness of this layer increases and at $x = 0.6$ the particle becomes completely paramagnetic. Mössbauer studies have shown that $Co_{0.8}Zn_{0.2}Fe_2O_4$ ($x = 0.2$) particles are in the superparamagnetic state and their magnetic blocking temperature is ~ 315 K, which is the most acceptable for the treatment of cancer by the magnetic hyperthermia method.

Keywords: $Co_xMn_{1-x}Fe_2O_4$, spinel ferrites, magnetic structure, superparamagnetism, Mossbauer spectroscopy, materials for biomedicine.

DOI: 10.21883/PSS.2023.03.55591.544

1. Introduction

Ceramic magnetic nanoparticles (MNPs) come into sharp focus due to their various applications, especially in biomedical sectors. The practical use of MNPs in different fields in the form of magnetic fluids (MF), for example as magnetic fluid seals, magnetic lubricants, visualization systems for the structure of permanent magnetic fields and the domain structure of magnetic materials, magnetically controlled light filters, hydromechanical transducers, etc. [1,2] requires a comprehensive studying of MNP properties. From the fundamental point of view, the understanding of MNP particles of nanoscale sizes is one of the main issues of magnetism.

MF is a stable colloid solution of a nonmagnetic fluid [3], where MNPs are suspended and controlled by an external magnetic field [4]. The most important are biomedical

applications of MFs, in particular: targeted delivery of drugs or diagnostic agents to indisposed organs [5,6], magnetic hyperthermic treatment of cancer by introducing MF into the tumor followed by heating of the MNP with alternating magnetic field, which results in destruction of cancerous cells in the indisposed organ [7–9]. Properties of a MF are determined by a combination of characteristics of its components (magnetic particles, dispersion medium and stabilizer), however the main component of the MF that forms its properties are magnetic and physical parameters of MNPs [8]. The extensive use of MFs is impeded to a significant extent by the lack of technologically simple and effective methods of synthesis of the main MF component, i.e. finely-dispersed MNPs with desired magnetic characteristics. The controlled synthesis of high-quality magnetic particles and studying of MNP properties are important from the scientific point of view and related to the understanding of the fundamentals of nanomagnetism [10]. The significant increase in the surface/volume ratio in MNPs leads to the formation of unique magnetic properties of MNPs, such as superparamagnetism; high saturation magnetization; spin glass state similar to freezing; high electrical resistance; high permittivity, etc. [11–13].

The most commonly used for biomedical applications superparamagnetic (SPM) MNPs of iron oxides (Fe_3O_4 magnetic iron, γ-Fe_2O_3 maghemite) [14–16] do not meet the requirements of modern biomedical sector, therefore MNPs with high magnetic characteristics are needed, which require comprehensive studying of MNP properties.

In recent years, the particles of AB_2O_4 spinel ferrites (SF), where $A = Mg^{2+}$, Fe^{2+}, Co^{2+}, Ni^{2+}, Cu^{2+}, Zn^{2+} and $B = Fe^{3+}$ and other metals denote divalent and trivalent cations, respectively, have attracted much attention of MNP developers) [16–23]. Among these materials the cobalt ferrite ($CoFe_2O_4$), a magnetically hard material with inverse structure, high coercive force (about 5.40 kOe), moderate saturation magnetization ($80\,emu \cdot g^{-1}$ at room temperature), high Curie temperature 520°C, prominent magnetocrystalline anisotropy, high magnetostriction coefficient, chemical stability and mechanical hardness, is paid the most attention as the most promising MNP for different healthcare applications, such as MRT, magnetic separation, delivery of drugs with magnetic control and cancer therapy using hyperthermia [18,20–27].

A shortcoming of $CoFe_2O_4$ MNPs for biomedical applications is their toxicity, therefore a number of studies (see [22] and references in this study) were focused on the toxicity reduction, for example, by doping with nontoxic ions, e.g. Zn [10,11,28–62]. It was shown that the doping of $CoFe_2O_4$ MNPs with Zn^{2+} ions in the range from 5 to 15% (in relation to Co) forms particles with increased hyperthermic efficiency, however further increase in Zn^{2+} quantity leads to the opposite effect [34]. In [38,39], $Co_{0.5}Zn_{0.5}Fe_2O_4$ MNPs of nearly spherical shape with an average size of particles equal to 13 nm for magnetic hyperthermia are obtained by the method of coprecipitation. The maximum specific absorption rate of 114.98 W/g was obtained in alternating magnetic field with a strength of 335.2 Oe, a frequency of 265 kHz, which is not higher than physiologically admissible parameters [39]. Doping of the cobalt spinel ($Co_{1-x}Zn_xFe_2O_4$) with Zn ions results in an increase in the saturation magnetization (M_s) at $0.2 \le x \le 0.4$ up to $\sim 100\,emu \cdot g^{-1}$ [52–54], which implies prospects of these MNPs for the hyperthermic treatment of cancer because the efficiency of hyperthermia depends heavily on the power of specific loss, which is approximately proportional to M_s. In the MNPs of $Co_{1-x}Zn_xFe_2O_4$ the presence of nanosize magnetic clusters in the infinite magnetic framework, cluster-paramagnetic phases, cluster glass, mixed magnetic phase, noncollinear spin structure and superparamagnetic clusters [9–11,21,26,29,42,56–60], is found together with the presence of mixed magnetic phase, which is rarely observed in this system [42,56]. However, despite the large number of publications devoted to investigations of $Co_{1-x}Zn_xFe_2O_4$ MNPs, some questions are still unanswered, such as, for example, the effect of increase in the quantity of introduced Zn ions on the magnetic structure of particles. The issue of magnetization strengthening in $Co_{1-x}Zn_xFe_2O_4$ MNPs is related to the cation exchange between nonequivalent sublattices A and B, with decrease in spin angularity in sublattice B and/or anisotropy caused by the deformation. To explain causes of the magnetization strengthening, a model of core-shell type was proposed, where the core and the shell have different magnetic structures ([61–63] and references in these studies). Such a particle is different from MNPs of the core-shell type, where the core and the shell are made of different magnetic materials [64]. Thus, a comprehensive investigation of structural, microstructural, magnetic and hyperfine properties of nanosize SFs is needed.

In this study the $Co_{1-x}Zn_xFe_2O_4$ MHPs synthesized by the method of coprecipitation with close average sizes were systematically investigated to study the effect of increased substitution by Zn^{2+} ions ($0.0 \le x \le 0.6$) on structural, microstructural, magnetic and hyperfine properties of ferrites of the $Co_{1-x}Zn_xFe_2O_4$ system. We used X-ray diffraction (XRD), Raman spectroscopy, magnetic measurements and Mössbauer spectroscopy to carry out the investigations.

2. Synthesis of $Co_{1-x}Zn_xFe_2O_4$ MNPs ($x = 0.0$, 0.1, 0.2, 0.4 and 0.6)

There is no one global method of MNP synthesis that could be prescribed for the combination of all desired chemical and physical characteristics. The method, which is eventually used, depends on the required combination of particle properties [11,34,35,54–68]. To obtain MNPs of the cobalt ferrite doped with Zn^{2+}, different methods have been used, such as hydrothermal synthesis, reaction of combustion, ball milling, coprecipitation, sol-gel, wet chemical sintering, spark plasma sintering and even a combination of these techniques with high-temperature annealing.

The microwave-assisted technique allows obtaining monodispersed particles within a shorter time. The sol-gel synthesis also allows obtaining low-dispersion MNPs, however extraction of particles from the gel imposes a problem, because it is difficult to clean the particle surface effectively. The electrospraying/depositing technique is an attractive method because the distribution of obtained particles by size is rather narrow and there are no active substances that need to be cleaned off. A heat treatment can increase the magnetization and blocking temperature of ferrite MNPs, however it leads to an undesirable increase in the particle size. It is of interest to note that MNPs of ferrites have demonstrated an improvement of magnetic parameters in the case of mechanical grinding [64]. The method of coprecipitation has a number of advantages: (i) low-cost and environment-friendly reagents are used instead of hazardous organic solvents; (ii) short time of the reaction; (iii) high crystallinity of particles; (iv) no special flushing procedures are required [9,13,37,38,39,48,54–56].

Based on the above said, the synthesis of MNPs of the $Co_{1-x}Zn_xFe_2O_4$ SF ($x = 0.0$, 0.1, 0.2, 0.4 and 0.6) was carried out by the method of chemical coprecipiation [57,13], modified by the authors [39]. We used chemically pure components: $FeCl_3 \cdot 6H_2O$ (97%), $CoCl_2 \cdot 6H_2O$ (97%), $ZnCl_2$ (99%) and sodium hydroxide (NaOH) without additional purification. To synthesize each composition of MNPs, the required quantities of $ZnCl_2$, $CoCl_{2.6} \cdot H_2O$ and $FeCl_3$ salts were dissolved in 200 ml of deionized water. The produced mixture was heated up to 80°C and 1N·NaOH solution was added in drops into it with continuous stirring to get pH of 12−13. Then the solution was heated at a temperature of 90°C for 60 min, which was sufficient to form the nanoparticles from hydroxides. The $Co_{1-x}Zn_xFe_2O_4$ MNPs were formed in accordance with the following reaction:

$$0.5(CoCl_2 \cdot 6H_2O) + 0.5(ZnCl_2) + 2(FeCl_3 \cdot 6H_2O) + 8(NaOH) \xrightarrow{80^\circ C} Co_{0.5}Zn_{0.5}Fe_2O_4 + 8NaCl + 19H_2O.$$

The synthesized MNPs were filtered and then flushed several times with deionized water, dried under an infrared lamp and the produced particles were used for the studies. The SEM-EDS analysis has shown that compositions of the produced MNPs of $Co_{1-x}Zn_xFe_2O_4$ are consistent with the components used for the synthesis ($x = 0.0$, 0.1, 0.2, 0.4 and 0.6).

3. Investigation techniques

Phase composition, structure and sizes of the synthesized crystallites were determined by profiles of X-ray diffraction patterns recorded by a Bruker XRD X-ray diffraction meter with CuK_α radiation and a wavelength of 1.542 Å in a 2θ range from 20 to 80°. The Raman spectra were obtained from nanoparticle granules using a NOST Raman scattering spectrometer composed of a solid-state laser with diode pumping, which operates at a wave length of 532 nm, and with a charge-coupled detector. Magnetic measurements in permanent magnetic field were carried out using the magnetometer with a vibrating sample in a Quantum Design measuring system. As a result, the saturation magnetization M_s, the coercive force H_c and the residual magnetization M_r were determined.

To investigate magnetic properties and magnetic structure, the Mössbauer spectroscopy was applied, which is an informative method of studying properties of materials [13,17,26,30,61–64]. The Mössbauer spectra (MS) were obtained using the ^{57}Fe isotope with recording of the γ-radiation in the geometry of transmission through the sample under study. The reference signal in the system of motion of the Doppler modulator in the spectrometer had a shape of triangle to set a speed with constant acceleration. The ^{57}Co with an activity of 20 mCi in the matrix of rhodium (Rh) served as a Mössbauer source of γ-radiation The speed scale was calibrated using α-iron foil at room temperature, and for a higher accuracy the calibration was carried out using a laser interferometer. The MS of investigated samples were obtained at room temperature. The spectra were mathematically processed by a program [65] that describes spectral lines by Lorentz shape peaks using the least square method. The divergence of theoretical values of the hyperfine interaction (HFI) parameters is determined from the statistical deviations. The routine of chi-square (χ^2) functional minimization in the program implements the search for optimal values of the parameters, i.e. width, intensities and positions of spectral lines on the speed scale. Positions of the spectral lines are used to calculate HFI parameters: IS — isomeric shift of Mössbauer lines, QS — quadrupole splitting, H_{eff} — effective magnetic field.

3.1. X-ray diffraction analysis of $Co_{1-x}Zn_xFe_2O_4$ MNPs ($x = 0.0$, 0.1, 0.2, 0.4 and 0.6)

X-ray patterns of $Co_{1-x}Zn_xFe_2O_4$ MNPs ($x = 0.1$, 0.2, 0.4 and 0.6) obtained immediately after the synthesis are shown in Fig. 1, *a*. It should be noted that X-ray patterns shown in Fig. 1 are similar to those presented, for example, in [21,26,36–38,42,68,69]. It can be seen in Fig. 1, *a*, that the synthesized powders of ferrites are single-phase substances because only the lines corresponding to the ferrite phase of cubic spinel are present in the obtained X-ray patterns and no any additional lines of other phases of ZnO, CoO and Fe_2O_3, that might be present due to the use of precursors and synthesis conditions, are found. The lines observed in the X-ray patterns (Fig. 1, *a*) are well matched with Miller indices of the cubic spinel structure of the $Fd3m$ space group and similar to those presented on the cards of the International Centre for Diffraction Data (ICDD) for $CoFe_2O_4$ (ICDD №00-022-1086) and $Co_{1-x}Zn_xFe_2O_4$ (ICDD №98-016-6201 through −6204). All diffraction peaks are wide due to the nanocrystal nature of ferrite particles. The X-ray patterns are used to obtain the

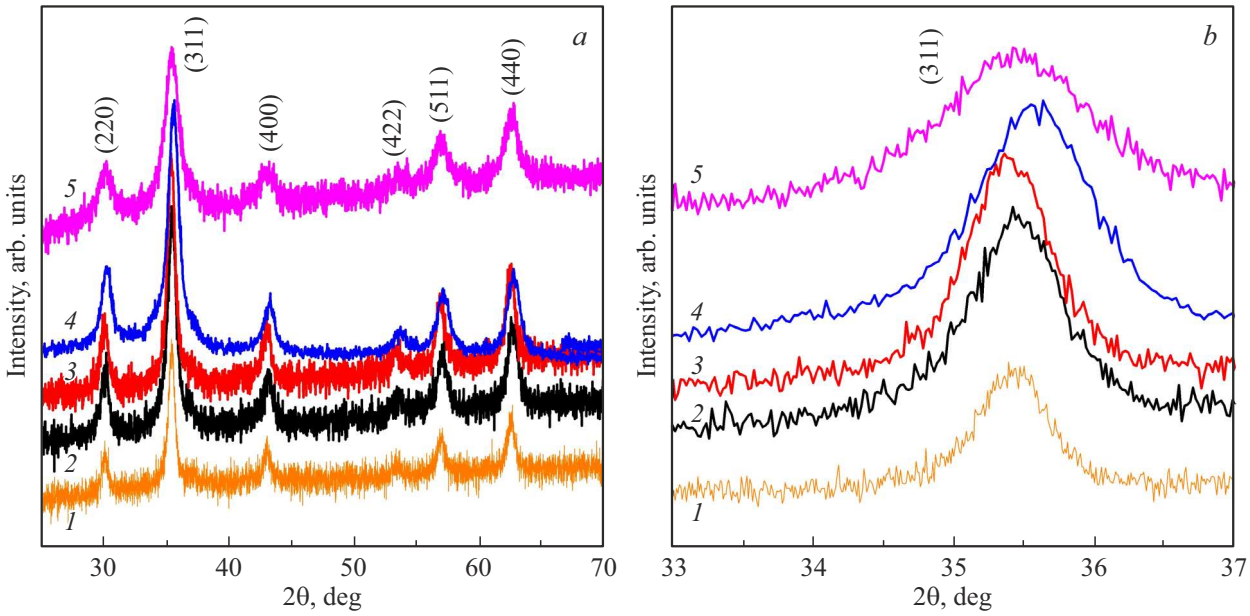

Figure 1. *a*) X-ray patterns of $Co_{1-x}Zn_xFe_2O_4$ nanoparticles, *b*) shift of position of the maximum intensity peak (311) depending on the quantity of Zn^{2+} ions. Numbers *1, 2, 3, 4* and *5* denote X-ray patterns of ferrites with Zn^{2+} ion substitutions of $x = 0.0$, 0.1, 0.2, 0.4 and 0.6, respectively.

lattice parameter and the mean size of crystallites. Lattice parameters of the lattice cell calculated by the least square method are presented in Table 1.

Such changes in the lattice parameters are related to the position of oxygen atoms, which is confirmed by results of other studies for similar systems [42]. The shift of position of diffraction peaks of the Zn-substituted Co ferrites, that is dependent on the composition, can be explained by the change in the lattice parameter of the lattice cell. Shift of the maximum intensity peak position (311) with a change in the quantity of Zn ions is shown in Fig. 1, *b*. Mean sizes of sample crystallites estimated by the Scherrer formula using X-ray diffraction patterns are in the range of 9–12 nm and, as can be seen from Table 1, decrease as the content of Zn^{2+} ions increases.

It can be seen from Table 1, that sizes of crystallites and lattice parameter decrease as the zinc concentration increases. The lattice parameter decreases from 8.452 Å for $CoFe_2O_4$ to 8.398 Å for $Co_{0.4}Zn_{0.6}Fe_2O_4$. The lattice parameter would seem to be increasing with increase in the zinc content, as it was observed in [69] and explained by the fact that the ion radius of zinc (0.88 Å) is greater than that of cobalt (0.83 Å) [70], therefore the lattice parameter grows with increase in the zinc content. The divergence between the data from Table 1 regarding the change in the lattice parameter and the results of [69] probably is due to the conditions used for the synthesis of samples. It can be stated on the basis of the X-ray diffraction data, that doping with zinc ions results in a change in particle size and structural properties, such as the lattice parameter and lengths of the bonds in tetrahedral and octahedral positions of the cubic spinel structure.

Table 1. Mean sizes of crystallites, lattice parameters and blocking temperature of $Co_{1-x}Zn_xFe_2O_4$ ferrites depending on the quantity of Zn^{2+} ions

Composite, x	Mean size, nm	Lattice constant, Å	Blocking temperature T_b, K	References
0.0	13.4	8.452	> 400	This work
0.1	12.1	8.412	> 400	″
0.2	10.1	8.393	368.8	″
0.4	9.2	8.371	276.7	″
0.6	7.0	8.398	150.9	″
$CoFe_2O_4$	9.3	8.586	–	[70]

3.2. Raman spectroscopy $Co_{1-x}Zn_xFe_2O_4$

Raman spectroscopy (Raman spectroscopy) is a technique to identify structural and oscillatory properties of SFs [71–76]. This non-destructive method is very sensitive to positions of cations that change appropriate oscillation modes and thus it allows studying: (i) the distribution of cations, (ii) the degree of inversion, i.e. the percentage of octahedral positions occupied by divalent cations in the SF, (iii) the doping/substitution of ferrites. It is known, that cobalt ferrites have an inverse spinel structure of the $O_{7h}(Fd_{3m})^{38}$ space group and according to the group theory the following optical phonon modes are expected: $5T_{1u} + A_{1g} + 1E_g + 3T_{2g}$ [73,74].

Table 2. Positions of lines on RS spectra of $Co_{1-x}Zn_xFe_2O_4$ MNPs

Composite, x	$A_{1g}(1)$	$A_{1g}(2)$	$T_{2g}(2)$	E_g
0.0	686.7	624.8	460.7	296.9
0.1	678.7	624.8	465.7	299.9
0.2	670.4	608.0	467.9	301.1
0.4	669.9	–	475.8	308.2
0.6	658.2	–	482.7	324.7

Raman (RS) spectra of $Co_{1-x}Zn_xFe_2O_4$ samples ($x = 0.0$, 0.1, 0.2, 0.4 and 0.6) recorded at room temperature with an excitation wavelength of 532 nm created by a solid-state laser are shown in Fig. 2. All Raman shifts and oscillation modes related to them are presented in Table 2.

There are three wide bands in RS spectra of all samples (Fig. 2): ~ 300, ~ 460 and $\sim 660\,cm^{-1}$, denoted in Fig. 2 as E_g, T_{2g} (2) and A_{1g}, which are generated by oscillations of oxygen and metal cations in octahedral and tetrahedral positions and correspond to the cubic crystal symmetry of the inverse spinel structure [71,75,76]. Some broadening of peaks is caused by the nanoscale dimensionality of crystallites [72,73]. The band in the region of $\sim 660\,cm^{-1}$ is related to the phonon mode A_{1g} and corresponds to a symmetrical stretching of the metal–oxygen bond in tetrahedral positions, while the band at $460\,cm^{-1}$ (is the phonon mode T_{2g} (2)), which is related to octahedral positions. The A_{1g} (2) band located at $\sim 615\,cm^{-1}$ is the main characteristic of inverse and mixed spinels and shows the degree of spinel inversion. This band is related to divalent cations (Co^{2+}) located in the tetrahedral position [71,72]. In the region of $\sim 555\,cm^{-1}$ in Fig. 2 there is no T_{2g} (3) high-frequency band arising due to the asymmetric deformation motion of oxygen coordinated with Co^{2+} in tetrahedral positions, as it is observed in [71,75,76]. This is possible due to the rough surface of the samples used to record the spectra. The T_{2g} (2) band at ~ 470 cm^{-1} is related to the oxygen atoms bound with Fe^{3+} ions that occupy octahedral positions (FeO_6). The E_g mode is related to the symmetric bend motion of oxygen anions in tetrahedral links of AO_4 [71]. The band observed in the region of $\sim 300\,cm^{-1}$ can be related to the phonon mode E_g that correlates with the metal–oxygen symmetric bend in the octa-sublattice [71,72,74]. The E_g phonon mode (in the region of $\sim 300\,cm^{-1}$) can be used to control the presence of Zn^{2+} ions in spinel structures, because depending on the Zn^{2+} content a shift and a change in the shape of this line was found, as can be seen in Fig. 2. With increase in the quantity of zinc the E_{g1} band shifts toward the blue side, probably because of changes in the cation distribution. In addition, the A_{1g} mode in $Co_{1-x}Zn_xFe_2O_4$ MNPs demonstrates a clearly seen broadening and a red shift in comparison to the pure $CoFe_2O_4$, as can be seen in Fig. 2.

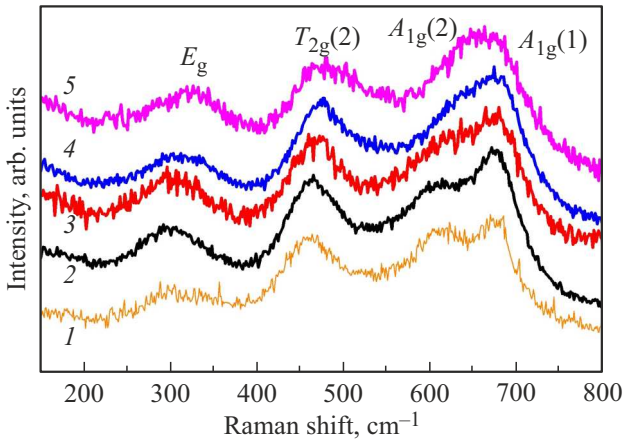

Figure 2. Raman spectra of $Co_{1-x}Zn_xFe_2O_4$ nanoparticles. Numbers *1, 2, 3, 4* and *5* denote spectra of ferrites with Zn^{2+} ion substitutions of $x = 0.0$, 0.1, 0.2, 0.4 and 0.6, respectively.

The $CoFe_2O_4$ bulk ferrite is an inverse spinel, where Co^{2+} ions occupy octahedral positions (the degree of inversion is 1), while the $ZnFe_2O_4$ should have a normal spinel structure, where all Zn^{2+} ions occupy tetrahedral nodes (the degree of inversion is 0). However, in the nanosize state these phases can have a partially inverse structure [45,72]. In particular, when zinc in the spinel substitutes cobalt, it is expected that Zn^{2+} ions are predominantly located on tetrahedral positions, while Fe^{3+} ions located in tetrahedral positions tend to occupy octahedral nodes; hence, the shift of the E_g phonon mode toward the blue side correlates with the Fe^{3+}.

The investigations described here are preliminary and quite complex. Therefore, for the correlation between the shift of the E_{g1} phonon mode and the quantity of Zn^{2+} ions of $Co_{1-x}Zn_xFe_2O_4$, further investigations are needed to obtain the calibration curve to study quantitative data of Zn^{2+} content in synthesized nanosize Co-ferrites.

3.3. Magnetic characteristics of $Co_{1-x}Zn_xFe_2O_4$ nanoparticles

Magnetic hysteresis (MH) loops of $Co_{1-x}Zn_xFe_2O_4$ MNPs shown in Fig. 3, *a* are obtained at room temperature with application of an external magnetic field in a range of from -2.0 to $+2.0$ T. Saturation magnetizations of $Co_{1-x}Zn_xFe_2O_4$ MNPs as a function of doping with Zn^{2+} ions are shown in Fig. 3, *b*. The $Co_{1-x}Zn_xFe_2O_4$ particles with $x = 0.0$ have maximum saturation magnetization, which decreases as the concentration of Zn^{2+} ions increases. The dependencies of MH obtained at 5 K for zero field cooling (ZFC) and cooling in an external magnetic field (FC) with a strength of 1 T are shown in Fig. 3, *c* and *d*, respectively. Curves of magnetization as a function of temperature (in a range of 5–400 K) for $Co_{1-x}Zn_xFe_2O_4$ samples in an external applied magnetic field of 1 T demonstrate a phase transition from the superparamagnetic

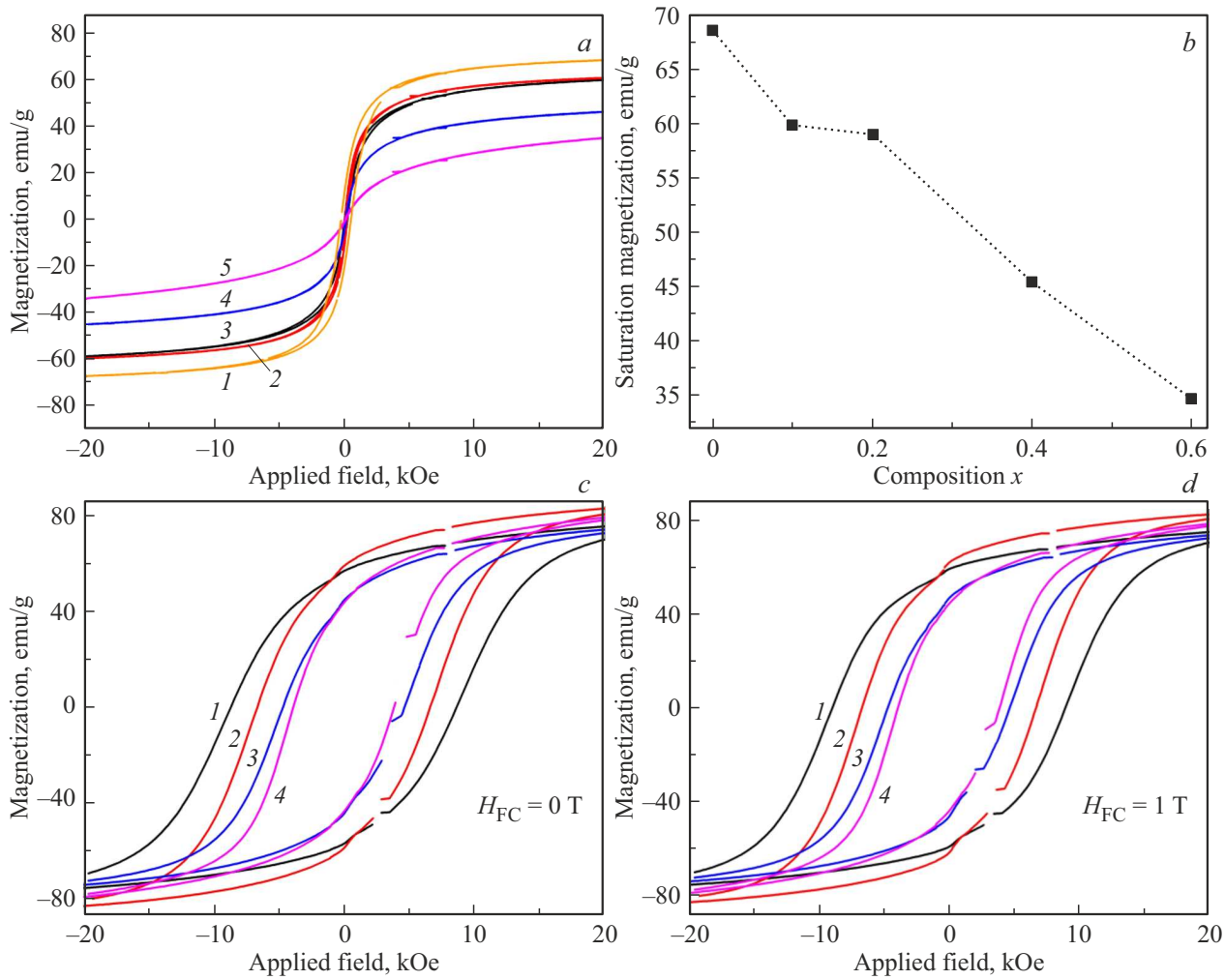

Figure 3. *a*) Magnetic hysteresis loops of $Co_{1-x}Zn_xFe_2O_4$ MNPs obtained at room temperature in the range of fields from −2.0 to +2.0 T. Here, numbers *1, 2, 3, 4* and *5* denote the curves obtained for $Co_{1-x}Zn_xFe_2O_4$ with Zn^{2+} ion substitutions of $x = 0.0$, 0.1, 0.2, 0.4 and 0.6, respectively; *b*) saturation magnetization depending on the concentration of *X* Zn^{2+} in $Co_{1-x}Zn_xFe_2O_4$ MNPs. Magnetic hysteresis loops obtained at room temperature for the cooling *c*) without external magnetic field (ZFC) and *d*) with an external magnetic field (FC) with a strength of 1 T. Here, numbers *1, 2, 3* and *4* denote the curves obtained for $Co_{1-x}Zn_xFe_2O_4$ with Zn^{2+} ion substitutions of $x = 0.1$, 0.2, 0.4 and 0.6, respectively.

state to the magnetically ordered state with a decrease in temperature (Fig. 3). The $Co_{1-x}Zn_xFe_2O_4$ particles with $x = 0.1$ and 0.2 demonstrate low coercive forces, while the compositions with $x = 0.4$ and 0.6 have zero coercivity and residual magnetization. In comparison to an unsubstituted sample of $CoFe_2O_4$, samples of the Zn-substituted cobalt ferrite are soft magnetic materials by virtue of their nature due to the low coercivity. With a decrease in temperature, a considerable increase in magnetization and coercive force is observed.

The magnetization in a SF with substituted metal ions depends on the nature of the introduced ions (magnetic or non-magnetic), their preference in the crystal lattice positions (A or B) and quantity of the introduced ions [29,38,73]. The higher magnetization related to the Zn-substituted ferrites can be explained by the fact that Zn^{2+} is a non-magnetic ion of a transition metal, which strongly prefers the tetrahedral position (A-position) almost in all known ferrites [29,38,71].

Fig. 4 shows temperature dependencies of magnetization obtained while cooling without any external magnetic field applied (ZFC) and with an external field with a strength of 1 kOe (FC). The Tb blocking temperatures obtained from the ZFC and FC curves (Fig. 4) are shown in Table 1, from which it can be seen that Tb for MNPs of $Co_{1-x}Zn_xFe_2O_4$ at $x > 0.4$ is below 300 K. It means, that MNPs of compositions with $x = 0.4$ and 0.6 are in the superparamagnetic state, while particles of the composition with $x = 0.1$ and 0.2 have their blocking temperature above the room temperature, which is explained by the combined effect of particle size and anisotropy.

Due to the magnetic anisotropy of nanoparticles, the magnetic moment usually has two stable orientations („easy axes“) antiparallel to each other and separated

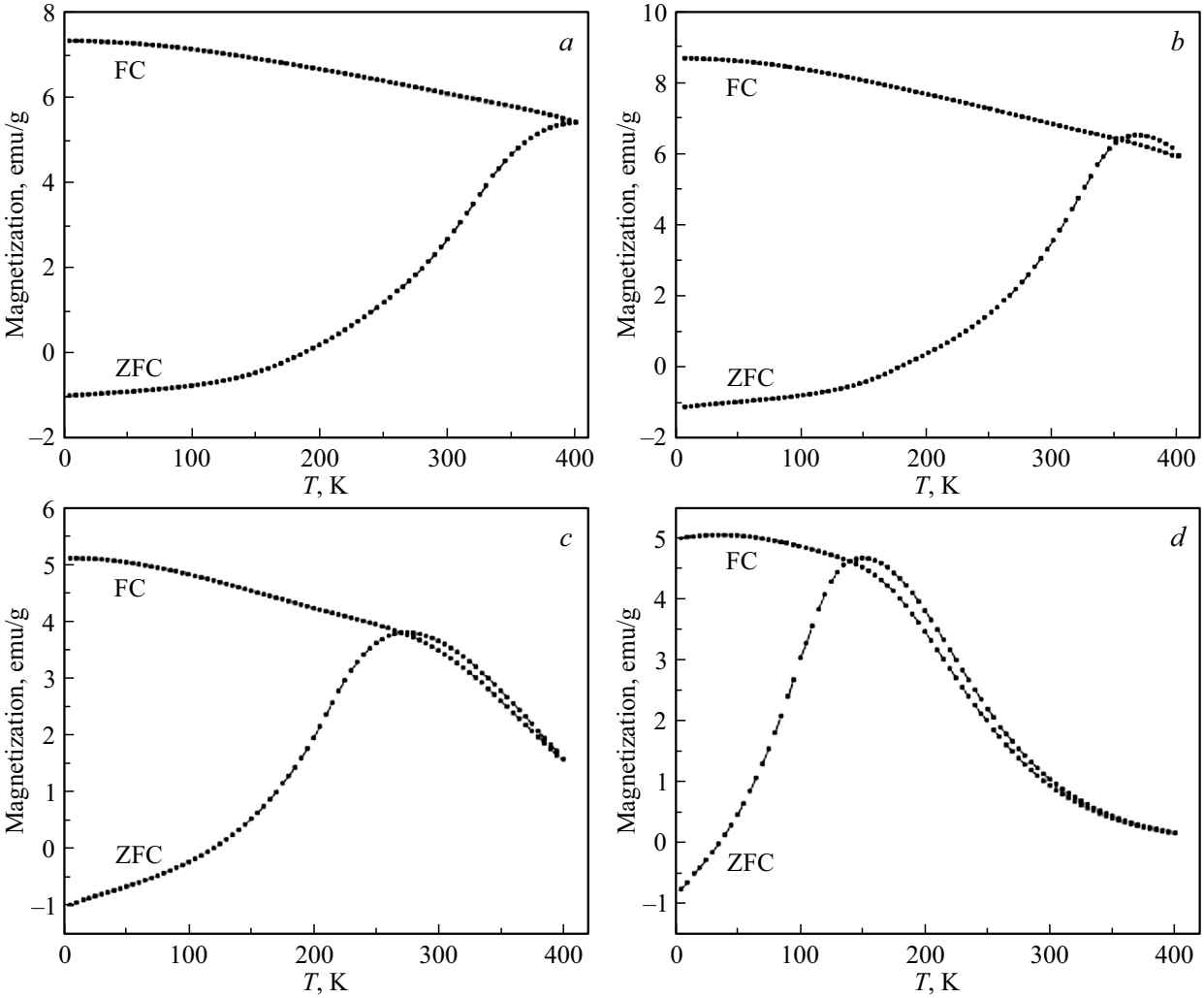

Figure 4. Temperature dependencies of magnetization for $Co_{1-x}Zn_xFe_2O_4$ MNPs obtained at room temperature while cooling without external magnetic field (ZFC) and with an external field (FC) with a strength of 1000 Oe. Here, letters *a, b, c* and *d* denote the dependencies for substitutions of $x = 0.1$, 0.2, 0.4 and 0.6, respectively.

by an energy barrier. With the final temperature, the magnetization can flip and change its direction. Mean time between two flips is known as Neel relaxation time and determined by the Neel–Arrhenius equation (1) [77]:

$$\tau_N = \tau_0 \exp\left(\frac{KV}{k_B T}\right). \quad (1)$$

Here: τ_N is the Neel relaxation time (mean time required for the random magnetization flip of a nanoparticle as a result of heat fluctuations); τ_0 is a time interval typical for the given material and known as „attempt time", which typical value is from 10^{-9} to 10^{-10} s; K is magnetic anisotropy constant; V is volume of the particle. Thus, KV is an energy barrier related to the motion of magnetization from its initial easy axis direction to another direction. k_B is Boltzmann constant, T is temperature. The interval of time τ_N can be from a few nanoseconds to years and even much longer and is a function of the grain volume, therefore the probability of flip becomes negligible for bulk materials or large particles.

The temperature of blocking the transition from superparamagnetic to blocked state is a function of temperature and determined by the following equation:

$$T_b = \frac{KV}{k_B \ln\left[\frac{\tau_m}{\tau_0}\right]}, \quad (2)$$

where τ_m is the time of measurement. Hence, in MNPs of $Co_{1-x}Zn_xFe_2O_4$, due to the large mean size and high magnetic anisotropy, particles with $x = 0.1$ will have their blocking temperature higher than those with $x = 0.2$ [78].

3.4. Mössbauer studies of $Co_{1-x}Zn_xFe_2O_4$ MNPs

The Mössbauer spectroscopy provides an important information on the phase composition, local electron configurations, magnetic structure and phenomena of magnetic relaxation of nanosize systems. The experimental

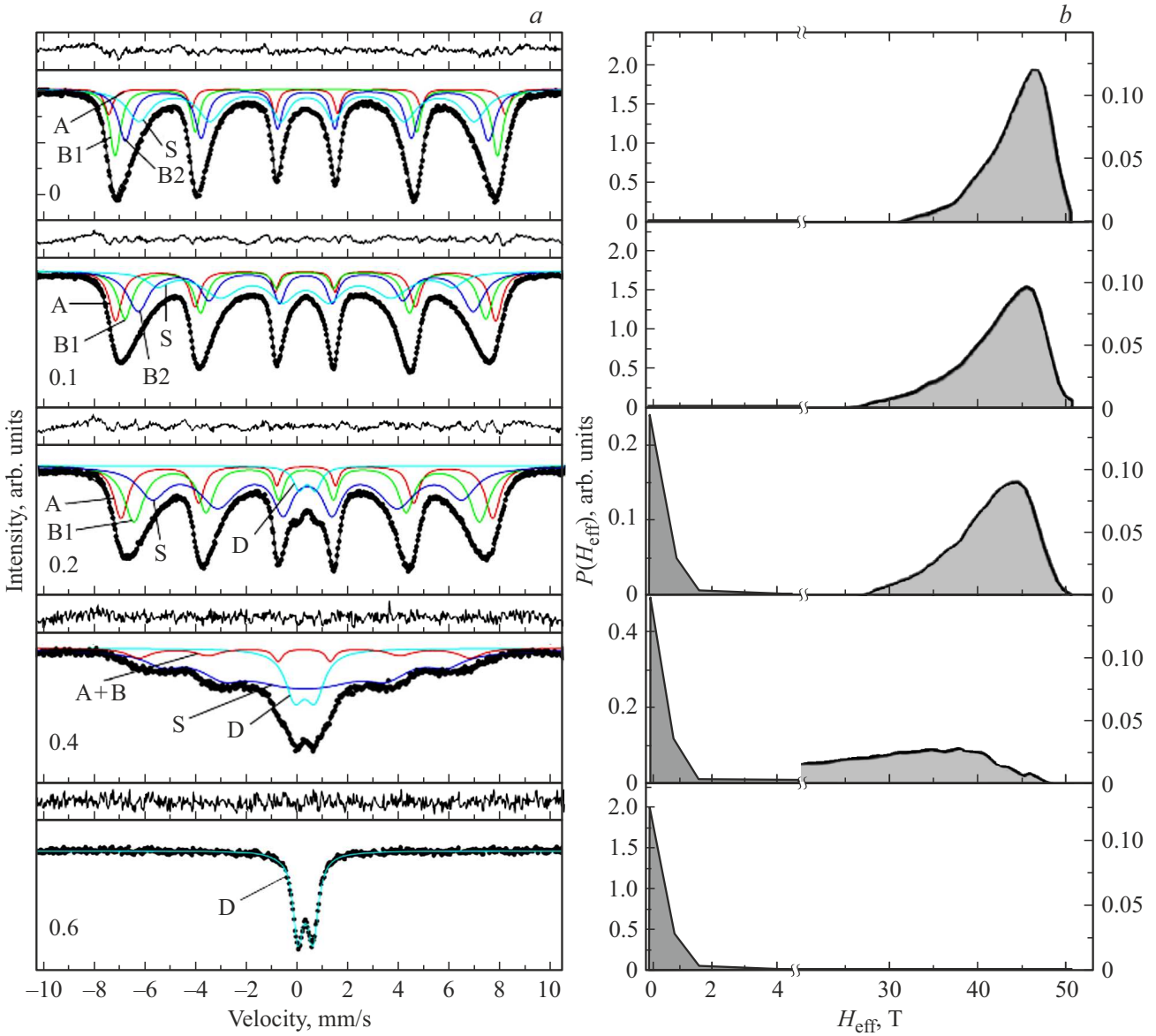

Figure 5. *a*) Mössbauer spectra of $Co_{1-x}Zn_xFe_2O_4$ MNPs obtained at room temperature. The experimental values are shown by dots, while the model components are shown by solid color lines: The sextuplet of Fe ions in A-positions is denoted by A letter and that of B-positions is denoted by B1, B2, the paramagnetic doublet is denoted by D (in accordance with colors). The sextuplet of Fe ions occupying positions in the surface layer is denoted as S. *b*) The distribution functions $P(H_{eff})$ extracted from experimental Mössbauer spectra of $Co_{1-x}Zn_xFe_2O_4$ MNPs using the fitting software program [65].

Mössbauer spectra (MS) of ^{57}Fe MNPs of $Co_{1-x}Zn_xFe_2O_4$ ferrite recorded at room temperature are shown in Fig. 5, *a*. As can be seen from Fig. 5, *a*, the experimental MS of $Co_{1-x}Zn_xFe_2O_4$ MNPs are composed of lines of Zeeman sextuplets (ZS) asymmetric toward the zero speed. With increase in the quantity of Zn ions from $x = 0.2$, doublet lines arise in the region of zero speeds on the background of ZS, and intensity of these doublets grows as the quantity of Zn ions increases. It should be noted, that the obtained MS of $Co_{1-x}Zn_xFe_2O_4$ MNPs (Fig. 5, *a*) are similar to those observed for $Co_{1-x}Zn_xFe_2O_4$ with appropriate quantities of Zn ions [30,35,40,45,68,79–84]. The MS of $CoFe_2O_4$ MNPs (Fig. 5, *a*) are significantly different from spectra of macrocrystalline ferrite, where Zeeman lines of sublattices (A) and [B] are resolved [85].

In MS of $Co_{1-x}Zn_xFe_2O_4$ MNPs (Fig. 5, *a*), the experimental values are shown by dots, while the model spectra, which are obtained by the mathematical processing of the experimental Mössbauer spectra by means of the fitting program [65], are shown by solid lines. Good compliance of the used models with the experimental Mössbauer spectra of the $Co_{1-x}Zn_xFe_2O_4$ MNPs is confirmed by minimum differences between the model and experiment values, which are shown above each spectrum and by the values

Table 3. Widths of the first and sixth lines (G) of the Zeeman splitting, as well as the isomer shifts (IS), the quadrupolar splittings (QS), the effective magnetic fields (H_{eff}) and the areas of lines (In) for the Fe ions in the tetrahedral (A) and octahedral (B) positions, in the surface layer (S) and of the doublets (D) in the $Co_{1-x}Zn_xFe_2O_4$ MNPs depending on the quantity of Zn (x) ions

x	Component	G, mm/s	IS, mm/s	QS, mm/s	H_{eff}, T	In, %
0.0	A	0.447 ± 0.026	0.321 ± 0.002	0.028 ± 0.004	48.12 ± 0.06	21
	B1	0.553 ± 0.039	0.309 ± 0.002	0.009 ± 0.003	46.26 ± 0.05	8
	B2	0.650 ± 0.055	0.315 ± 0.002	0.017 ± 0.004	44.01 ± 0.07	29
	S	1.222 ± 0.031	0.338 ± 0.004	0.017 ± 0.008	40.96 ± 0.15	42
0.1	A	0.505 ± 0.016	0.315 ± 0.001	0.019 ± 0.003	46.91 ± 0.04	12
	B1	0.615 ± 0.029	0.303 ± 0.001	0.017 ± 0.003	44.84 ± 0.04	18
	B2	0.897 ± 0.039	0.319 ± 0.002	-0.004 ± 0.003	42.04 ± 0.05	27
	S	1.231 ± 0.028	0.332 ± 0.003	0.020 ± 0.005	37.77 ± 0.11	43
0.2	A	0.688 ± 0.020	0.309 ± 0.002	0.020 ± 0.003	45.41 ± 0.04	19
	B1	0.933 ± 0.049	0.303 ± 0.002	0.020 ± 0.004	42.21 ± 0.06	32
	S	1.322 ± 0.032	0.343 ± 0.004	0.019 ± 0.007	37.83 ± 0.12	45
	D	0.564 ± 0.024	0.343 ± 0.005	0.649 ± 0.012	–	4
0.4	A+B	1.125 ± 0.135	0.314 ± 0.010	0.013 ± 0.020	40.51 ± 0.27	11
	S	1.560 ± 0.221	0.338 ± 0.013	0.005 ± 0.020	34.62 ± 0.39	70
	D	0.915 ± 0.027	0.331 ± 0.004	0.794 ± 0.011	–	19
0.6	D	0.503 ± 0.006	0.336 ± 0.002	0.576 ± 0.004	–	100

of χ^2 within the interval of $1.0-1.2$. The HFI parameters in Table 3 are calculated using the positions of spectral lines in MS of $Co_{1-x}Zn_xFe_2O_4$ MNPs.

The isomer shifts (IS) are shown relative to the α-Fe metal foil. Impurity (secondary) phases of iron oxides in the materials under study should be manifested in MS of $Co_{1-x}Zn_xFe_2O_4$ as additional ZS or doublets, with different HFI parameters. Therefore, any impurity phase in an amount not less than 3 at.% of iron can be easily detected from the MS. The analysis of the experimental MS of $Co_{1-x}Zn_xFe_2O_4$ MNPs (Fig. 5, *a*) has not shown secondary phase lines; hence, there are no impurities in the MNPs under study, which matches the XRD and Raman spectroscopy data.

The spectral lines of Fe^{2+} and Fe^{3+} ions are reliably identified in Mössbauer spectroscopy data by their chemical shifts, that are equal to $\sim 0.2-0.5$ mm/s for Fe^{3+} and $\sim 0.9-1.1$ mm/s for Fe^{2+} [13]. However, in the case of SF MNPs, the IS values of iron ions in the high-spin state of Fe^{3+}, as a rule, are in the range of $0.3-0.6$ mm/s. Table 3 shows IS values for Fe^{3+} ions in the tetrahedral A and octahedral B-positions in the $Co_{1-x}Zn_xFe_2O_4$ MNPs depending on the substitution value. As can be seen from Table 3, IS values for Fe ions in [B]- and (A)-positions are almost the same and do not depend on the quantity of Zn ions, which is indicative of the insensitivity of s-electrons of the Fe^{3+} ions to the quantity of Zn. There are no high values of chemical shifts (from 0.9 to 1.1 mm/s) of the Fe ions in the Fe^{2+} low-spin state in the MS of $Co_{1-x}Zn_xFe_2O_4$. The range of IS values for A- and B-positions is within $0.3-0.5$ mm/s, indicating that in the $Co_{1-x}Zn_xFe_2O_4$ MNPs under study there are only iron ions in the high-spin state, Fe^{3+}.

In Fig. 5, *a*, as well as in the majority of published studies of ferrites, the MS are composed of ZS lines asymmetrically broadened toward the zero speed, which is indicative of the presence of several Zeeman subspectra formed due to different possible configurations of the nearest neighbors of Fe^{3+} ions occupying nonequivalent positions [87,88]. The asymmetric broadening of Zeeman lines observed in the MS is related to the distribution of the hyperfine field caused by the random placement of Fe and Zn ions over the crystal lattice positions, described by the following binomial distribution [35,87,88]:

$$P(k) = \binom{n}{k} p^k (1-p)^{n-k}, \quad n = 6, k = 0, \ldots, 6, \quad (3)$$

where $P(k)$ is the probability of Zn atoms presence in the amount of k in the nearest surrounding of Fe atoms from the sublattice B, and p corresponds to the probability of Zn atoms presence in the sublattice A, in our case $p = x$. The presence of three different cations

(iron, cobalt and manganese) in the samples under study significantly increases the chance of random distribution of these cations, thereby leading to formation of several octahedral [B]-positions with different occupancies. The Fe^{3+} ions in (A)-positions usually have no effective field distribution because Fe ions of (A)-sites have no atoms of Zn as their nearest neighbors. This is related to the preference of Zn^{2+} ions to occupy positions in the (A)-sublattice, while Co^{2+} ions tend to occupy [B] sites. Therefore, in the MS only one ZS is related to Fe atoms in (A)-positions. The A−B superexchange interaction is determined by the hyperfine fields of the ions in (A)-positions, which have twelve adjacent neighbors in [B]-positions and, therefore has less dependence on the random distribution of cations in B-sites. The nearest neighbors of Fe ions in [B]-positions are only six cations in (A)-positions and the random cation distribution over these positions has much stronger effect on the hyperfine fields of Fe ions of [B]-sites. In other words, a change in the cation distribution over B-positions affects the A-position only by 1/12, whereas a change in the cation distribution over A-positions leads to the changes in the B-sublattice by 1/6 [89]. Covalence of the Fe(A)−O bond is higher than that of Fe[B]−O, which qualitatively explains why the transfer of spin density from (A) to [B] in the spinel structure is more effective than the transfer in the reverse direction [89]. In addition, the hyperfine magnetic field of Fe ions of the (A)-sublattice in the SF is higher than the field of Fe^{3+} ions in B-positions [13,26,35,87]. As a result, in ferrites the effective magnetic field sensed by the Fe^{3+} ions in (A)-positions is independent from the distribution of magnetic ions over [B]-sites, while the hyperfine field of Fe ions in [B]-positions is strongly dependent on the nearest neighborhood of ions in (A)-positions.

Based on the above, to process the MS of $Co_{1-x}Zn_xFe_2O_4$ MNPs, models were used that are composed of sextuplets and a doublet, which gave a satisfactory description of the experimental MS of $Co_{1-x}Zn_xFe_2O_4$ MNPs by the χ^2 criterion. A ZS is observed in MS of $Co_{1-x}Zn_xFe_2O_4$ MNPs with $x = 0$. With $x = 0.2$, a low-intensity quadrupole doublet (4%) arises in the MS on the background of ZS (96%), where intensity increases as the quantity of Zn ions grows, while the intensity of sextuplet decreases, and with $x = 0.6$ only the paramagnetic doublet is observed in the MS. Such changes in the MS of $Co_{1-x}Zn_xFe_2O_4$ MNPs with increase in the concentration of Zn ions are explained by the superparamagnetic relaxation [26,81]. If the relaxation time τ of nanoparticles is less than the measurement time ($\tau_m = 10^{-7}$ s for ^{57}Fe), then the MS are composed of a doublet. With $\tau \gg \tau_m$ the ZS is observed in the MS with a good resolution of absorption lines.

In [17] authors reported a paramagnetic doublet observed in the MS of $Mg_xZn_{1-x}Fe_2O_4$ MNPs on the background of two ZS, one of which had a good resolution, while lines of the second sextuplet were not resolved because absorption lines of this sixtuplet were considerably wider than widths of lines in the first sixtuplet, and the effective field was considerably smaller. Two such different sixtuplets observed in the MS were explained in [17] by the presence of two types of particles in the sample, in particular: the sixtuplet with a good resolution is indicative of the presence of particles with magnetic ordering in the sample with $\tau \gg \tau_m$, while the sixtuplet with wide unresolved lines is related to particles that are in the superparamagnetic state ($\tau \ll \tau_m$). Two different ZS are observed due to the different distribution of cations and formation of two types of particles in the sample. However, it is hardly likely that in samples synthesized by a certain method that are single-phase samples with well crystallized particles, as it is shown by X-ray diffraction studies, there are two groups of particles of different types.

The QS values (Table 3) of nonequivalent positions of iron ions in the studied MNPs of $Co_{1-x}Zn_xFe_2O_4$ SF within an experiment error are close to zero (except for QS for the doublets), which is indicative of maintaining the cubic symmetry of Fe^{3+} ions and their environment. The QS value of doublets less than 0.8 mm/s indicates that in the $Co_xMn_{1-x}Fe_3O_2$ MNPs the Fe ions are also in the Fe^{3+} high-spin state, because for the Fe^{2+} ions in the low-spin state the QS value is significantly higher.

Blocking temperature T_b is determined from the MS as a temperature, where areas of sixtuplets and the paramagnetic doublet are equal to each other. Results of the analysis of areas of the spectral lines of components in the MS of $Co_{1-x}Zn_xFe_2O_4$ MNPs (Table 2) allows stating that with increase in the content of Zn ions T_b decreases and with $x = 0.6$ it becomes lower than the room temperature, which matches the data of magnetic measurements.

The relation of the observed sixtuplets (Fig. 5, *a*) to iron ions occupying (A)- and [B]-sublattices was determined by the magnitude of effective magnetic fields. The sixtuplet with the highest effective field is related to Fe ions of the (A)-sublattice, and other sixtuplets with similar widths of absorption lines, but with lower effective fields are related to Fe ions in [B]-sites with contributions determined by binominal distribution (3).

As can be seen in Fig. 5, *a*, in addition to (A) and [B] sextuplets in the MS of $Co_{1-x}Zn_xFe_2O_4$ MNPs, a sixtuplet is observed, which is denoted as S in Fig. 5, *a*, with effective fields less than the fields of iron ions in (A)- and [B]-positions and with lines considerably wider than those of other sixtuplets. It should be noted, that similar MS with sixtuplet lines asymmetric toward the zero speed were observed, for example, in [30,35,40,45,68,79–84,92–95], however this fact was left unexplained.

Let us consider the causes of S ZS formation in the MS of $Co_{1-x}Zn_xFe_2O_4$ MNPs. One of contributions is provided by the Fe ions, which nearest neighbors are magnetic ions in an amount less than that of the iron ions in B1 and B2 positions. As known, with a decrease in particle size the surface/volume ratio increases multiple times, that considerably changes the superexchange interactions of iron

ions occupying positions in the surface and near-surface layers of nanoparticles and lost part of the nearest magnetic neighbors [91]. This can result in the formation of canting orientations of spin moments on the MNP surface [92–95] or the formation of „magnetically dead" or spin-glass surface layer [21] that reduces the magnetization and temperature of magnetic ordering of MNPs. Hence, the contribution to sixtuplet S also is provided by the iron ions located on the surface and in the near-surface layer of MNP and lost some superexchange bonds due to the surface presence. Thus, the evolution of MS of $Co_{1-x}Zn_xFe_2O_4$ MNPs when doping with Zn ions can be explained as follows. The existence of a „magnetically dead" on the surface of $CoFe_2O_4$ ($x = 0$) MNPs is refuted by the fact that no paramagnetic doublet is observed in the MS (Fig. 5, *a*). The existence of a magnetic structure in MNPs of MFe_2O_4 ferrites (where M is a metal ion), which essence consists in that the particle body has a structure of spinel with colinear arrangement of spins of Neel type is shown in [21,33,61,63,86,92–95] by Mössbauer studies in strong external magnetic fields. (It should be noted, that the existence of canting spin structure in a thin surface layer of macroscopic crystals was first shown by the authors of [96].) Therefore, an assumption can be made that with decrease in size of particles the canting spin structure in the surface layer is kept.

The introduction of a small quantity of Zn ($x > 0.2$) results in an additional destruction of superexchange bonds in the surface layer of $Co_{1-x}Zn_xFe_2O_4$ particles and in the MS (Fig. 5, *a*) a paramagnetic doublet arises that is indicative of the transition of a thin surface layer to the paramagnetic state. The destruction of exchange bonds due to the surface also leads to a decrease in the effective fields on Fe ions of the near-surface layer. With increase in the quantity of the substituting ions, thickness of this paramagnetic layer increases and gradually captures ever-deeper near-surface layers of the shell. With $x = 0.6$ all the particle of $Co_{1-x}Zn_xFe_2O_4$ becomes completely paramagnetic at room temperature.

The observed in $Co_{1-x}Zn_xFe_2O_4$ MNP, and, by extension, also in other particles of SF, state with different magnetic structures of the body and surface layer can not de identified, for example, by methods of electron microscopy or other methods, except for the method of Mössbauer spectroscopy. This is related to the fact that MNPs of SF are synthesized by a certain method, are single-phase and well crystallized and composed of one material. The latter makes the SF particles different from MNPs of the core-shell type, where the core and the shell are made of different magnetic materials, for example, magnetic iron and maghemite [62]. Thus, based on the results of Mössbauer studies, it can be stated that the body and the surface layer of $Co_{1-x}Zn_xFe_2O_4$ nanoparticles ($0 \le x \le 0.6$) have different magnetic structures.

3.5. Distribution functions of effective magnetic fields $P(H_{\text{eff}})$ for $Co_{1-x}Zn_xFe_2O_4$

The use of Lorentz lines to process the MS in order to study the distribution of the effective magnetic field $P(H_{\text{eff}})$ arising due to the local nonuniformity of cation distribution is not effective in the case if sixtuplets are unresolved. If Fe ions are surrounded by different types of local chemical medium, the most reliable is the method of MS processing with the use of Voigt function as a spectral line [97,98]. Therefore, from the experimental MS of $Co_{1-x}Zn_xFe_2O_4$ MNPs the $P(H_{\text{eff}})$ functions shown in Fig. 5, *b* were recovered using the program of [65]. The obtained $P(H_{\text{eff}})$ functions differ from the $P(H_{\text{eff}})$ curve of the SF macrocrystals, where two maxima of iron ions in two nonequivalent sublattices are observed.

In the $P(H_{\text{eff}})$ functions obtained for $Co_{1-x}Zn_xFe_2O_4$ MNPs (Fig. 5, *b*) before $x < 0.4$, a peak is observed in the region of fields from 43 to 47 T, which is asymmetric toward lower fields. The range from 0 to 1.6 T corresponds to doublet lines in the MS, which are related to the part of particles in the paramagnetic state and whose probability of presence is increasing, as can be seen in Fig. 5, *b*, as the quantity of Zn ions is increasing in $Co_xMn_{1-x}Fe_2O_4$ MNPs. The $P(H_{\text{eff}})$ curves observed within the range from 45 T and below (Fig. 5, *b*), are related to the ZS lines with different environments. With increase in the quantity of substituting ions of Zn (Fig. 5, *b*), the probability of ZS presence decreases and position of the maximum shifts toward low effective fields, indicating that the substitution with Zn ions leads to a decrease in H_{eff} and in the percentage of magnetically ordered state, while the percentage of paramagnetic phase increases. With $x = 0.6$, only a line of paramagnetic phase is observed in the $P(H_{\text{eff}})$ function, which is indicative of MNPs transition to the paramagnetic state.

Thus, features of $P(H_{\text{eff}})$ functions (Fig. 5, *b*) reflect the complex magnetic structure of the $Co_{1-x}Zn_xFe_2O_4$ MNPs under study, which can not be explained only by the redistribution of Zn ions surrounding iron ions and the effect of surface has to be taken into consideration.

3.6. Estimation of sizes of $Co_{1-x}Zn_xFe_2O_4$ MNPs

The analysis of the experimental MS of $Co_{1-x}Zn_xFe_2O_4$ MNPs and published results of Mössbauer studies allows estimating the sizes of $Co_{1-x}Zn_xFe_2O_4$ MNPs under study. For MNPs of $CoFe_2O_4$ with sizes of 1−3 nm [99,100], sizes of 2 and 3 nm [101], 4.6 and 5.7 nm [102], 7.8 nm [103] the MS were obtained that are composed of doublets, which are indicative of the paramagnetic states of particles. In MS of $CoFe_2O_4$ MNPs with sizes from 8 to 30 nm, in particular, with sizes of 8.85 nm [68], 22 nm [103], 25 nm [104] and 30 nm [105], ZS are observed with well resolved lines, indicating that particles in this range of sizes are in the magnetically-ordered phase. In [106] for MNPs of $CoFe_2O_4$ with sizes of 7.8 nm and [68] for MNPs

of $Co_{0.5}Zn_{0.5}Fe_2O_4$ with sizes of 13.26 nm the MS are obtained, which are indicative of the superparamagnetic state of particles. In [100] for MNPs of $CoFe_2O_4$ with sizes of 9.2 and 13.8 nm the existence of ZS and a paramagnetic doublet is observed in the MS. The comparison between the literature data and the experimental MS of $Co_{1-x}Zn_xFe_2O_4$ MNPs allows stating that sizes of the studied particles are within the range from 8 to 14 nm, which is consistent with the X-ray diffraction data.

4. Conclusion

The systematic studies of $Co_{1-x}Zn_xFe_2O_4$ MNPs are carried out depending on the concentration of Zn ions ($x = 0.0$, 0.1, 0.2, 0.4, 0.6) synthesized by the simple method of coprecipitation. The structural and morphological properties of the MNPs are studied by means of the X-ray diffraction (XRD), the transmission electron microscopy, the Raman and Mössbauer spectroscopy. The structural XRD-analysis and the data of the Raman and Mössbauer spectroscopy confirm that the studied particles are single-phase and have a cubic structure of spinel ferrite (SF) $Co_{1-x}Zn_xFe_2O_4$ (space group $Fd3m$) within the whole range of the substitution by the Zn ions. It is found by the Raman spectroscopy method, that $CoFe_2O_4$ MNPs are structured as a normal spinel and when being doped by the Zn^{2+} ions, the Co^{2+} and Fe^{3+} cations are redistributed between tetrahedral and octahedral positions and the structure converts to the mixed ferrite. Based on the X-ray diffraction and Mössbauer data, it is found that mean sizes of the crystallites are in the range from 8 to 14 nm depending on the amount of substitution with Zn ions. The experimental Mössbauer spectra are indicative of the typical superparamagnetic behavior of the $Co_{1-x}Zn_xFe_2O_4$ MNPs. The introduction of Zn ions into the $Co_{1-x}Zn_xFe_2O_4$ results, with $x > 0.1$, in the transition to the paramagnetic state of a thin layer on the surface of particles, where of the thickness increases as the quantity of introduced Zn ions increases and at $x \ge 0.6$ all the particle becomes paramagnetic.

Based on the Mössbauer studies an important information was obtained for the first time without application of external magnetic field regarding the magnetic structure of SF nanoparticles, the difference between the magnetic structure of the particle's body and surface layer. In the body part of the $CoFe_2O_4$ ($x = 0$) ferrite a colinear ordering of spin moments is observed, while in the surface layer spin moments have a canting structure due to the effect of surface. The mechanism of SF MNPs evolution from the magnetically-ordered to paramagnetic state with introduction of paramagnetic ions is described for the first time. The results obtained for SF MNPs are important for the development and creation of magnetic nanoparticles for different applications, including biomedical ones.

Funding

I.M. Obaidat and B. Issa would like to thank the University of Sharjah and the Sharjah Research Academy for grant №2101050262 for joint research activities.

Conflict of interest

The authors declare that they have no conflict of interest.

References

[1] J.A. Ramos-Guivar, E.O. Lopez, J.-M. Greneche, F.J. Litterst, E.C. Passamani. Appl. Surf. Sci. **538**, 148021 (2021). https://doi.org/10.1016/j.apsusc.2020.148021
[2] M. Abdolrahimi, M. Vasilakaki, S. Slimani, N. Ntallis, G. Varvaro, S. Laureti, C. Meneghini, K.N. Trohidou, D. Fiorani, D. Peddis. Nanomater. **11**, *7*, 1787 (2021). https://doi.org/10.3390/nano11071787
[3] S.A. Novopashin, M.A. Serebryakova, S.Ya. Khmel. Teplofizika i aeromekhanika **22**, *4*, 411 (2015) (in Russian).
[4] M.A.A. Kerroum, C. Iacovita, W. Baaziz, D. Ihiawakrim, G. Rogez, M. Benaissa, C.M. Lucaciu, O. Ersen. Int. J. Mol. Sci. **21**, *20*, 27775 (2020). DOI: 10.3390/ijms21207775
[5] E.M. Materon, C.M. Miyazaki, O. Carr, N. Joshi, P.H.S. Picciani, C.J. Dalmaschio, F. Davis, F.M. Shimizu. Appl. Surf. Sci. Adv. **6**, 100163 (2021). DOI: https://doi.org/10.1016/j.apsadv.2021.100163
[6] M.G.M. Schneider, M.J. Martín, J. Otarola, E. Vakarelska, V. Simeonov, V. Lassalle, M. Nedyalkova. Pharmaceutics **14**, *1*, 204 (2022). https://doi.org/10.3390/pharmaceutics14010204
[7] I.M. Obaidat, V. Narayanaswamy, S. Alaabed, S. Sambasivam, C.V.V.M. Gopi. Princip. Magn. Hyperthermia. Magnetochemistry **5**, *4*, 67 (2019). DOI: 10.3390/magnetochemistry5040067
[8] X. Yu, S. Ding, R. Yang, C. Wu, W. Zhang. Ceram. Int. **47**, *5*, 5909 (2021). https://doi.org/10.1016/j.ceramint.2020.11.049
[9] M. Veverka, P. Veverka, Z. Jirák, O. Kaman, K. Knížek, M. Maryško, E. Pollert, K. Závěta. J. Magn. Magn. Mater. **322**, *16*, 2386 (2010). https://doi.org/10.1016/j.jmmm.2010.02.042
[10] A.V. Nikam, B.L.V. Prasad, A.A. Kulkarni. Cryst. Eng. Commun. **20**, *35*, 5091 (2018).
[11] K. Sarkar, R. Mondal, S. Dey, S. Majumder, S. Kumar. J. Magn. Magn. Mater. **487**, 165303 (2019).
[12] V. Narayanaswamy, I.A. Al-Omari, A.S. Kamzin, B. Issa, H.O. Tekin, H. Khourshid, H. Kumar, A. Mallya, S. Sambasivam, I.M. Obaidat. Nanomater. **11**, *5*, 1231 (2021). https://doi.org/10.3390/nano11051231
[13] A.S. Kamzin, I.M. Obaidat, V.G. Semenov,, V. Narayanaswamy, I.A. Al-Omari, B. Issa, I.V. Buryanenko, FTT **64**, *6*, 712 (2022). DOI: 10.21883/FTT.2022.06.52406.298
[14] S. Ranoo, B.B. Lahiri, S.P. Damodaran, J. Philip. J. Mol. Liquids **360**, 119444 (2022). https://doi.org/10.1016/j.molliq.2022.119444
[15] I.M. Obaidat, B. Issa, Y. Haik. Nanomater. **5**, *1*, 63 (2015). DOI: 10.3390/nano5010063
[16] U.M. Engelmann, A.A. Roeth, D. Eberbeck, E.M. Buhl, U.P. Neumann, T. Schmitz-Rode, I. Slabu. Sci. Rep. **8**, 13210 (2018). DOI: 10.1038/s41598-018-31553-9

[17] E. Umut, M. Coşkun, H. Güngüneş, V. Dupuis, A.S. Kamzin. J. Supercond. Nov. Magn. **34**, *3*, 913 (2021). https://doi.org/10.1007/s10948-020-05800-y
[18] A. Manohar, D.D. Geleta, C. Krishnamoorthi, J. Lee. Ceram. Int. **46**, *18*, 28035 (2020).
[19] S.M. Hoque, M.S. Hossain, S. Choudhury, S. Akhter, F. Hyder. Mater. Lett. **162**, 60 (2016). http://dx.doi.org/10.1016/j.matlet.2015.09.066
[20] M. Liu, M. Lu, L. Wang, S. Xu, J. Zhao, H. Li. J. Mater. Sci. **51**, *11*, 5487 (2016). DOI: 10.1007/s10853-016-9853-3
[21] G. Lavorato, M. Alzamora, C. Contreras, G. Burlandy, F.J. Litterst, E. Baggio-Saitovitch. Particle **39**, *4*, 1900061 (2019). https://doi.org/10.1002/ppsc.201900061
[22] K.K. Kefeni, T.A.M. Msagati, T.T. Nkambule, B.B. Mamba. Mater. Sci. Eng. C **107**, 110314 (2020). https://doi.org/10.1016/j.msec.2019.110314
[23] F.G. da Silva, J. Depeyrot, A.F.C. Campos, R. Aquino, D. Fiorani, D. Peddis. J. Nanosci. Nanotechnol. **19**, *8*, 4888 (2019).
[24] O. Cadar, T. Dippong, M. Senila, E.-A. Levei. „Progress, Challenges and Opportunities in Divalent Transition Metal-Doped Cobalt Ferrites Nanoparticles Applications", Ch. 5. In: Advanced Functional Materials / Eds N. Tasaltin, P.S. Nnamchi, S. Saud. IntechOpen (2020). DOI: 10.5772/intechopen.93298
[25] Z. Karimi, L. Karimi, H. Shokrollahi. Mater. Sci. Eng. C **33**, *5*, 2465 (2013). https://doi.org/10.1016/j.msec.2013.01.045
[26] Q. Lin, J. Xu, F. Yang, J. Lin, H. Yang, Y. He. Materials **11**, *10*, 1799 (2018). DOI: 10.3390/ma11101799
[27] G. Baldi, D. Bonacchi, C. Innocenti, G. Lorenzi, C. Sangregorio. J. Magn. Magn. Mater. **311**, *1*, 10 (2007). https://doi.org/10.1016/j.jmmm.2006.11.157
[28] R.S. Yadav, J. Havlica, M. Hnatko, P. Šajgalík, C. Alexander, M. Palou, E. Bartoníčková, M. Boháč, F. Frajkorová, J. Masilko, M. Zmrzlý, L. Kalina, M. Hajdúchová, V. Enev. J. Magn. Magn. Mater. **378**, 190 (2015). https://doi.org/10.1016/j.jmmm.2014.11.027
[29] S.S. Jadhav, S.E. Shirsath, S.M. Patange, K.M. Jadhav. J. Appl. Phys. **108**, *9*, 093920 (2010).
[30] F. Nakagomi, P.E.N. de Souza, T.J. Castro, V.K. Garg, A.C. Oliveira, F.C.E. Silva, A. Franco Jr, P.C. Morais, S.W. da Silva. J. Alloy. Compd. **842**, 155751 (2020). https://doi.org/10.1016/j.jallcom.2020.155751
[31] B.N. Pianciola, E. Lima, H.E. Troiani, L.C.C.M. Nagamine, R. Cohen, R.D. Zysler. J. Magn. Magn. Mater. **377**, 44 (2015). https://doi.org/10.1016/j.jmmm.2014.10.054
[32] H.L. Andersen, C. Granados-Miralles, M. Saura-Muzquiz, M. Stingaciu, J. Larsen, F. Søndergaard-Pedersen, J.V. Ahlburg, L. Keller, C. Frandsen, M. Christensen. Mater. Chem. Front. **3**, *4*, 668 (2019).
[33] A. Omelyanchik, K. Levada, S. Pshenichnikov, M. Abdolrahim, M. Baricic, A. Kapitunova, A. Galieva, S. Sukhikh, L. Astakhova, S. Antipov, B. Fabiano, D. Peddis, V. Rodionova. Materials **13**, *21*, 5014 (2020). DOI: 10.3390/ma13215014
[34] M. Albino, E. Fantechi, C. Innocenti, A. López-Ortega, V. Bonanni, G. Campo, F. Pineider, M. Gurioli, P. Arosio, T. Orlando, G. Bertoni, C. De Julián Fernández, A. Lascialfari, C. Sangregorio. J. Phys. Chem. C **123**, *10*, 6148 (2019). https://doi.org/10.1021/acs.jpcc.8b10998
[35] T. Tatarchuk, N. Paliychuk, M. Pacia, W. Kaspera, W. Macyk, A. Kotarba, B.F. Bogacz, A.T. Pedziwiatr, I. Mironyuk, R. Gargula, P. Kurzydło, A. Shyichuk. New J. Chem. **43**, *7*, 3038 (2019).
[36] V. Mameli, A. Musinu, A. Ardu, G. Ennas, D. Peddis, D. Niznansky, C. Sangregorio, C. Innocenti, T.K. Nguyen, C.C. Thanh. Nanoscale **8**, *19*, 10124 (2016). DOI: 10.1039/c6nr01303a
[37] M. Schmidt, H.L. Andersen, C. Granados-Miralles, M. Saura-Múzquiz, M. Stingaciu, M. Christensen. Dalton Trans. **45**, *15*, 6439 (2016). https://doi.org/10.1039/c5dt04701c
[38] D.S. Nikam, S.V. Jadhav, V.M. Khot, R.A. Bohara, C.K. Hong, S.S. Mali, S.H. Pawar. RSC Adv. **5**, *3*, 2338 (2015). https://doi.org/10.1039/c4ra08342c
[39] A.S. Kamzin, D.S. Nikam, S.H. Pawar. Phys. Solid State 59, 156 (2017) DOI: 10.1134/S1063783417010127
[40] A. Ramakrishna, N. Murali, Tulu Wegayehu Mammo, K. Samatha, V. Veeraiah. Physica B: Condens. Matter. **534**, 134 (2018). https://doi.org/10.1016/j.physb.2018.01.033
[41] A. Manikandan, L. John Kennedy, M. Bououdina, J. Judith Vijaya. J. Magn. Magn. Mater. **349**, 249 (2014). https://doi.org/10.1016/j.jmmm.2013.09.013
[42] I. Sharifi, H. Shokrollahi. J. Magn. Magn. Mater. **324**, *15*, 2397 (2012). https://doi.org/10.1016/j.jmmm.2012.03.008
[43] G. Barrera, M. Coisson, F. Celegato, S. Raghuvanshi, F. Mazaleyrat, S.N. Kane, P. Tiberto. J. Magn. Magn. Mater. **456**, 372 (2018). https://doi.org/10.1016/j.jmmm.2018.02.072
[44] P. Coppola, F.G. da Silva, G. Gomide, F.L.O. Paula, A.F.C. Campos, R. Perzynski, C. Kern, J. Depeyrot, R. Aquino. J. Nanopart. Res. **18**, *5*, 138 (2016). https://doi.org/10.1007/s11051-016-3430-1
[45] T.R. Tatarchuk, M. Bououdina, N.D. Paliychuk, I.P. Yaremiy, V.V. Moklyak. J. Alloy. Compd. **694**, 777 (2017). https://doi.org/10.1016/j.jallcom.2016.10.067
[46] R.N. Bhowmik, R. Ranganathan. J. Magn. Magn. Mater. **248**, *1*, 101 (2002).
[47] H. Parmar, P. Acharya, R.V. Upadhyay, V. Siruguri, S. Rayaprol. Solid State Commun. **153**, *1*, 60 (2013). https://doi.org/10.1016/j.ssc.2012.09.021
[48] R.V. Upadhyay, H. Parmar, P. Acharya, A. Banerjee. Solid State Commun. **163**, 50 (2013). https://doi.org/10.1016/j.ssc.2013.02.020
[49] S. Dey, A. Roy, J. Ghose, R.N. Bhowmik, R. Ranganathan. J. Appl. Phys. **90**, *8*, 4138 (2001). https://doi.org/10.1063/1.1401798
[50] T. Dippong. Nanomater. (Basel) **12**, *1*, 107 (2022).
[51] S. Amiri, H. Shokrollahi. Mater. Sci. Eng. C **33**, *1*, 1 (2013). https://doi.org/10.1016/j.msec.2012.09.003
[52] T. Dippong, O. Cadar, E.A. Levei, I.G. Deac. J. Magn. Magn. Mater. **498**, 166168 (2020). https://doi.org/10.1016/j.jmmm.2019.166168
[53] G.V. Duong, N. Hanh, D.V. Linh, R. Groessinger, P. Weinberger, E. Schafler, M. Zehetbauer. J. Magn. Magn Mater. **311**, *1*, 46 (2007). https://doi.org/10.1016/j.jmmm.2006.11.167
[54] Y.H. Hou, Y.J. Zhao, Z.W. Liu, H.Y. Yu, X.C. Zhong, W.Q. Qiu, D.C. Zeng, L.S. Wen. J. Appl. Phys. **109**, *7*, 07A502 (2011). https://doi.org/10.1063/1.3535442
[55] T.I. Shabatina, O.I. Vernaya, V.P. Shabatin, M.Ya. Melnikov. Magnetochemistry **6**, *3*, 30 (2020). DOI: 10.3390/magnetochemistry6030030

[56] I. Sharifi, H. Shokrollahi. J. Magn. Magn. Mater. **334**, 36 (2013). https://doi.org/10.1016/j.jmmm.2013.01.021
[57] E.A. Périgo, G. Hemery, O. Sandre, D. Ortega, E. Garaio, F. Plazaola, F.J. Teran. Appl. Phys. Rev. **2**, *4*, 041302 (2015). DOI: 10.1063/1.4935688
[58] X. Huang, J. Zhang, W. Wang, T. Sang, B. Song, H. Zhu, W. Rao, C. Wong. J. Magn. Magn. Mater. **405**, 36 (2016). https://doi.org/10.1016/j.jmmm.2015.12.051
[59] S. Dey, S.K. Dey, S. Majumder, A. Poddar, P. Dasgupta, S. Banerjee, S. Kumar. Physica B **448**, 247 (2014). https://doi.org/10.1016/j.physb.2014.03.073
[60] F. Sharifianjazi, M. Moradi, N. Parvin, A. Nemati, A.J. Rad, N. Sheysi, A. Abouchenari, A. Mohammadi, S. Karbasi, Z. Ahmadi, A. Esmaeilkhanian, M. Irani, A. Pakseresht, S. Sahmani, M. Shahedi Asl. Ceram. Int. **46**, *11*, Part B, 18391 (2020).
[61] V. Šepelák, A. Feldhoff, P. Heitjans, F. Krumeich, D. Menzel, F.J. Litterst, I. Bergmann, K.D. Becker. Chem. Mater. **18**, *13*, 3057 (2006).
[62] A.S. Kamzin, I.M. Obaidat, A.A. Valliulin, V.G. Semenov, I.A. Al-Omari. Phys. Solid State **62**, *11*, 2167 (2020). DOI: 10.1134/S1063783420110153
[63] S. Morup, J.A. Dumesic, H. Topsøe. In: Mössbauer spectroscopy applications / Ed. R.L. Cohen. Academic, N.Y. (1990). P. 1.
[64] V. Kuncser, O. Crisan, G. Schinteie, F. Tolea, P. Palade, M. Valeanu, G. Filoti. Modern Trends in Nanoscience. Editura Academiei Romane, Bucharest (2013). V. 197.
[65] V.G. Semenov, V.V. Panchuk. The Mössbauer Spectra Processing MossFit software. Private message, 2010. (in Russian).
[66] P.N. Anantharamaiah, H.M. Shashanka, R. Kumar, J.A. Chelvane, B. Sahoo. Mater. Sci. Eng. B **266**, 115080 (2021).
[67] K.M. Batoo, E.H. Raslan, Y. Yang, S.F. Adil, M. Khan, A. Imran, Y. Al-Douri. AIP Advances **9**, *5*, 055202 (2019). https://doi.org/10.1063/1.5078411
[68] M.M. Kothawale, R. Pednekar, U.B. Gawas, S.S. Meena, N. Prasad, S. Kumar. J. Supercond. Nov. Magn. **30**, *2*, 395 (2017).
[69] H. Kiswanto, A. Puspitasari, E. Suharyadi, T. Kato, S. Iwata. IOP Conf. Ser.: Mater. Sci. Eng. **367**, *1*, 012001 (2018). DOI: 10.1088/1757-899X/367/1/012001
[70] P. Roy, S.M. Hoque, S.I. Liba, S. Choudhury. AIP Advances **8**, *10*, 105124 (2018). DOI: 10.1063/1.5040890
[71] V. Bartůněk, D. Sedmidubský, Š. Huber, M. Švecová, P. Ulbrich, O. Jankovský. Materials **11**, *7*, 1241 (2018). DOI: 10.3390/ma11071241
[72] N. Monni, V. Mameli, S.A. Sahadevan, S. Gai, C. Cannas, M.L. Mercuri. J. Nanosci. Nanotechnol. **19**, *8*, 5043 (2019). DOI: 10.1166/jnn.2019.16792
[73] M. Testa-Anta, M.A. Ramos-Docampo, M. Comesaña-Hermo, B. Rivas-Murias, V. Salgueiriño. Nanoscale Adv. **1**, *6*, 2086 (2019). DOI: 10.1039/C9NA00064J
[74] J.P. Singh, R.C. Srivastava, H.M. Agrawal, R. Kumar. J. Raman Spectrosc. **42**, *7*, 1510 (2011).
[75] P.N. Anantharamaiah, P.A. Joy. Phys. Chem. Chem. Phys. **18**, *15*, 10516 (2016).
[76] P.N. Anantharamaiah, P.A. Joy. J. Phys. D **50**, *43*, 435005 (2017).
[77] S. Ota, Y. Takemura. J. Phys. Chem. C **123**, *47*, 28859 (2019). DOI: 10.1021/acs.jpcc.9b06790
[78] V. Narayanaswamy, I.A. Al-Omari, A.S. Kamzin, B. Issa, H.O. Tekin, H. Khourshid, H. Kumar, A. Mallya, S. Sabasivam, I.M. Obaidat. Nanomater. **11**, *5*, 1231 (2021). https://doi.org/10.3390/nano11051231
[79] M. Hashim, S.S. Meena, R.K. Kotnala, S.E. Shirsath, P. Bhatt, S. Kumar, E. Şentürk, R. Kumar, N. Gupta, Alimuddin. J. Magn. Magn. Mater. **360**, 21 (2014). http://dx.doi.org/10.1016/j.jmmm.2014.01.047
[80] M.I.A. Abdel Maksoud, A. El-Ghandour, G.S. El-Sayyad, R.A. Fahim, A.H. El-Hanbaly, M. Bekhit, E.K. Abdel-Khalek, H.H. El-Bahnasawy, M.A. Elkodous, A.H. Ashour, A.S. Awed. J. Inorg. Organometallic Polymers. Materials **30**, *9*, 3709 (2020).
[81] S.C. Bhargava, P.K. Iyengar. Phys. Status Solidi B **53**, *1*, 359 (1972). https://doi.org/10.1002/pssb.2220530138
[82] R.S. de Biasi, L.H.G. Cardoso. Physica B **407**, *18*, 3893 (2012). http://dx.doi.org/10.1016/j.physb.2012.06.017
[83] J.Z. Msomi, W.B. Dlamini, T. Moyo, P. Ezekiel. J. Magn. Magn. Mater. **373**, 68 (2015). DOI: 10.1016/j.jmmm.2014.01.044
[84] B.F. Bogacz, R. Gargula, P. Kurzydło, A.T. Pedziwiatr, T. Tatarchuk, N. Paliychuk. Acta Phys. Polonica A **134**, *5*, 993 (2018).
[85] A. Bouhas, M. Amzal, B. Zouranen. Mater. Chem. Phys. **33**, *1–2*, 80 (1993). https://doi.org/10.1016/0254-0584(93)90094-3
[86] Coey, J.M.D. Physical Review Letters **27** (17), 1140 (1971).
[87] G.A. Sawatzky, F. Van Der Woude, A.H. Morrish. Phys. Rev. **187**, *2*, 747 (1969).
[88] S. Dey, S.K. Dey, B. Ghosh, P. Dasgupta, A. Poddar, V.R. Reddy, S. Kumar. J. Appl. Phys. **114**, *9*, 093901 (2013). https://doi.org/10.1063/1.4819809
[89] F. Van Der Woude, G.A. Sawatzky. Phys. Rev. B **4**, *9*, 3159 (1971).
[90] E. Wu, S.J. Campbell, W.A. Kaczmareka, M. Hofmann, S.J. Kennedy. Int. J. Mater. Res. **94**, *10*, 1127 (2003).
[91] I.M. Obaidat, V. Mohite, B. Issa, N. Tit, Y. Haik. Cryst. Res. Tech. **44**, *5*, 489 (2009). DOI: 10.1002/crat.200900022
[92] R.H. Kodama, A.E. Berkowitz, E.J. McNiff, S. Foner. J. Appl. Phys. **81**, *8*, 5552 (1997). DOI: 10.1063/1.364659
[93] K. Haneda, A.H. Morrish. J. Appl. Phys. **63**, *8*, 4258 (1988). DOI: 10.1063/1.340197
[94] J. Marx, H. Huang, K.S.M. Salih, W.R. Thiel, V. Schünemann. Hyperfine Interact. **237**, *1*, 41 (2016). DOI: 10.1007/s10751-016-1241-5
[95] N. Velinov, E. Manova, T. Tsoncheva, C. Estournès, D. Paneva, K. Tenchev, V. Petkova, K. Koleva, B. Kunev, I. Mitov. Sol. St. Sci. **14**, 1092 (2012). Doi.10.1016/j.solidstatesciences.2012.05.023.
[96] A.S. Kamzin. J. Experim. Theoretical Phys. **89**, *5*, 890 (1999).
[97] M.E. Matsnev, V.S. Rusakov. AIP Conf. Proc. **1489**, *1*, 178 (2012).
[98] G.N. Konygin, O.M. Nemtsova, V.E. Porsev. Zhurn. priklad. spektroskopii **86**, *3*, 374 (2019). (in Russian).
[99] E.J. Choi, Y. Ahn, S. Kim, D.H. An, K.U. Kang, B.-G. Lee, K.S. Baek, H.N. Oak. J. Magn. Magn. Mater. **262**, *1*, L198 (2003).
[100] Y. Kim, D. Kim, C. Lee. Physica B **337**, *1–4*, 42 (2003). DOI: 10.1016/S0921-4526(03)00322-3
[101] N. Moumen, P. Bonville, M.P. Pileni. J. Phys. Chem. **100**, *34*, 14410 (1996).

[102] S.W. Lee, C.S. Kim. J. Magn. Magn. Mater. **303**, *2*, e315 (2006). https://doi.org/10.1016/j.jmmm.2006.01.042
[103] H.H. Hamdeh, W.M. Hikal, S.M. Taher, J.C. Ho, N.P. Thuy, O.K. Quy, N. Hanh. J. Appl. Phys. **97**, *6*, 064310 (2005). DOI: 10.1063/1.1856219
[104] S.M. Patange, S.S. Desai, S.S. Meena, S.M. Yusuf, S.E. Shirsath. RSC Adv. **5**, *111*, 91482 (2015).
[105] G. Chandra, R.C. Srivastava, V.R. Reddy, H.M. Agrawal. J. Magn. Magn. Mater. **427**, 225 (2017). http://dx.doi.org/10.1016/j.jmmm.2016.10.082
[106] M. Ristic, S. Krehula, M. Reissner, M. Jean, B. Hannoyer, S. Musić. J. Mol. Structure **1140**, 32 (2017).

Translated by Y.Alekseev